Earth and Planetary Science Letters 391 (2014) 319–326

Contents lists available at ScienceDirect

Earth and Planetary Science Letters

www.elsevier.com/locate/epsl

Structure-controlled seismic anisotropy along the Karadere–Düzce branch of the North Anatolian Fault revealed by shear-wave splitting tomography

Zefeng Li [a,b], Haijiang Zhang [a,*], Zhigang Peng [b]

[a] Laboratory of Seismology and Physics of Earth's Interior, School of Earth and Space Sciences, University of Science and Technology of China, Hefei, Anhui 230026, China

[b] School of Earth and Atmospheric Sciences, Georgia Institute of Technology, Atlanta, GA 30332, United States

ARTICLE INFO

Article history:
Received 30 September 2013
Received in revised form 27 January 2014
Accepted 30 January 2014
Available online 22 February 2014
Editor: P. Shearer

Keywords:
shear wave splitting
anisotropy mechanism
North Anatolian Fault
fault zone imaging

ABSTRACT

We use a three-dimensional (3D) shear-wave splitting (SWS) tomography method developed by Zhang et al. (2007) to map the spatial distribution of crustal anisotropy in the Karadere–Düzce branch of the North Anatolian Fault (NAF) in western Turkey. The input data consists of 20751 measurements of the SWS delay times from 7856 aftershocks of the 1999 Mw 7.4 İzmit and Mw 7.1 Düzce earthquakes. The results show a continuous belt-like highly anisotropic zone along the Karadere-Düzce branch of NAF, generally ~3 km wide and down to ~5 km deep. The observed asymmetric pattern of anisotropy along the Karadere segment is qualitatively consistent with asymmetric damages from the unilateral eastward propagation of the İzmit rupture. Another strong anisotropy region was found near the end of the İzmit rupture zone, close to the dipping direction of the fault segment that ruptured during the subsequent Düzce earthquake. These results are generally consistent with the shallow fault-zone anisotropy inferred from previous studies. While the anisotropy generally becomes weaker at depth and/or outside the fault zone, we also identify several highly anisotropic regions as deep as ~10 km, primarily within the Almacik block. These isolated anisotropy regions could be explained by individual intrusive igneous rock bodies with different mineral alignment. Overall, seismic anisotropy in upper crust of the Karadere-Düzce branch of the NAF is structurally controlled.

1. Introduction

Seismic shear waves propagating through anisotropic media are expected to separate into fast and slow components, a phenomenon termed shear wave splitting (SWS). In the upper crust, shear wave anisotropy is widely observed and usually considered as a result of preferential alignment of fluid-filled cracks in rocks or sediments (Crampin and Booth, 1985; Leary et al., 1990; Crampin, 1991; Zhang and Schwartz, 1994). In this case, the fast polarization direction is parallel to the maximum horizontal compressive stress direction due to alignment of preexisting cracks in that direction. Other mechanisms are mainly structurally controlled, including preferential mineral alignment, sedimentary bedding planes, and alignments along active fault zones (Boness and Zoback, 2006).

Generally two SWS parameters are measured: polarization direction of the fast component and delay time δt between the fast and slow components. While visual inspection was used to measure SWS parameters in many earlier studies (Crampin, 1990), automated methods are needed to obtain a large data set of SWS measurements. These include the cross-correlation method (e.g., Fukao, 1984; Liu et al., 2003), the covariance matrix (CM) method (e.g., Silver and Chan, 1991), and the aspect ratio (AR) method (Shih et al., 1989). To understand spatial distribution of crustal anisotropy, many studies simply average the SWS parameters at each station and superimpose them on the station location (e.g., Boness and Zoback, 2006; Yang et al., 2011). Other recent studies have proposed to plot the average measurements at the earthquake source region (e.g., Peng and Ben-Zion, 2004), or somewhere between the source and receivers (e.g., Liu et al., 2008). When plotting the rose diagrams of fast polarizations on stations, Eken et al. (2013) showed that stricter quality criteria can lead to preferred fast polarization more clearly, which might result from near-station anisotropic bodies. However, in all these cases, the exact location and magnitude of the anisotropy zone along the ray path remain unclear.

Various efforts have been made to map the spatial distribution of anisotropy. For example, Audoine et al. (2004) developed a

* Corresponding author. Tel.: +86 551 6360 3428.
E-mail address: zhang11@ustc.edu.cn (H. Zhang).

http://dx.doi.org/10.1016/j.epsl.2014.01.046
0012-821X/

method to produce spatial average of splitting parameters by dividing the source–receiver paths into many grid points. More rigorous anisotropy tomography methods have also been proposed to image the spatial distribution of anisotropy (e.g., Abt and Fischer, 2008; Long et al., 2008). However, complicated waveforms pose difficulties in inversion due to the nonlinear effect of multiple layers of anisotropy (e.g., Silver and Savage, 1994). Long et al. (2008) developed a 2.5D SWS intensity tomography method to study upper mantle anisotropy, which calculates sensitivity kernels for heterogeneously anisotropic media. In their method, splitting intensity measured from long period SKS waves, instead of standard splitting delay time and fast polarization, is used to image the anisotropy structure. In comparison, Abt and Fischer (2008) imaged 3D anisotropy structure in upper mantle using the SWS parameters by assuming the anisotropy is caused by the lattice-preferred orientation of olivine and orthopyroxene. Partial derivatives of fast polarization and delay time with respect to the orientation of olivine α-axis and anisotropy strength are numerically calculated by modeling splitting parameters for a synthetic wavelet using the Christoffel equation.

Recently, Zhang et al. (2007) developed an SWS tomography method to map the spatial distribution of anisotropy in upper crust by back projecting the splitting delay times along ray paths derived from known 1D or 3D velocity models. Comparing with other techniques (e.g., Long et al., 2008; Abt and Fischer, 2008), this method does not handle the anisotropic direction in the inversion and the partial derivative of delay time with respect to anisotropy percentage is calculated using ray theory. In this simplified method, all measurements of station–event pairs are utilized in the inversion and weighted by an objective parameter, such as the waveform cross-correlation coefficient between slow and fast shear waves. However, so far it has only been used in the Parkfield section of the San Andreas Fault to map the 3D anisotropy distribution, where 3D velocity models have been well developed (e.g., Thurber et al., 2006).

In this study, we apply the same method to the Karadere–Düzce branch of the North Anatolian Fault (NAF) in northern Turkey. The NAF is the active transform boundary between the Eurasian and the Anatolian Plates. Several earlier studies have found clear crustal anisotropy near the epicentral region of the 1999/08/17 Mw 7.4 İzmit earthquake that ruptured the western segment of the NAF (Crampin and Booth, 1985; Evans et al., 1985). Peng and Ben-Zion (2004) analyzed the SWS parameters in Karadere–Düzce branch of the NAF ruptured during the İzmit earthquake and the 1999/12/12 Mw 7.1 Düzce earthquake. They found predominant fault-parallel fast directions for stations within a 1 km broad zone around the rupture zones of the two recent earthquakes. Hurd and Bohnhoff (2012) used several stations in a larger region around the NAF and found similar results.

In this study, we use the SWS tomography method (Zhang et al., 2007) to map the spatial distribution of anisotropy around the Karadere–Düzce of the NAF, based on the SWS parameters measured by Peng and Ben-Zion (2004). Our results, which will be presented below, are generally consistent with the previous observations, but contain more quantitative information on the along-strike and depth extent of crustal anisotropy in this region.

2. Data selection

We use the SWS measurements (Peng and Ben-Zion, 2004) from numerous aftershocks recorded by 31 stations (Fig. 1). Specifically, a temporary 10-station PASSCAL seismic network covered a 6-month period after the İzmit earthquake on August 17, 1999. 7 additional stations were deployed for the first 2 weeks after the İzmit mainshock, and another 14-station array was deployed across the Karadere branch of the NAF for the last 2-week period. A total

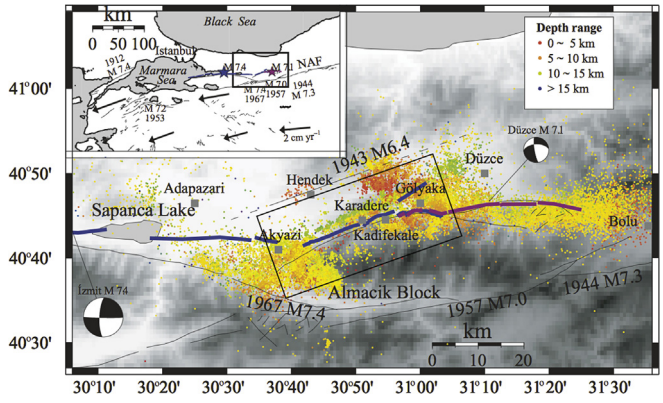

Fig. 1. Map of study region. Epicentral distribution of ~26 000 earthquakes recorded by the PASSCAL seismic experiment along the Karadere–Düzce branch of the NAF. Aftershock locations are marked with colors denoting different depth ranges. The surface ruptures of the İzmit and Düzce earthquakes are indicated with thick blue and purple lines, respectively. The box marks the SWS tomography region. The inset illustrates the tectonic environment in northwestern Turkey. After Peng and Ben-Zion (2004). (For interpretation of the references to color in this figure legend, the reader is referred to the web version of this article.)

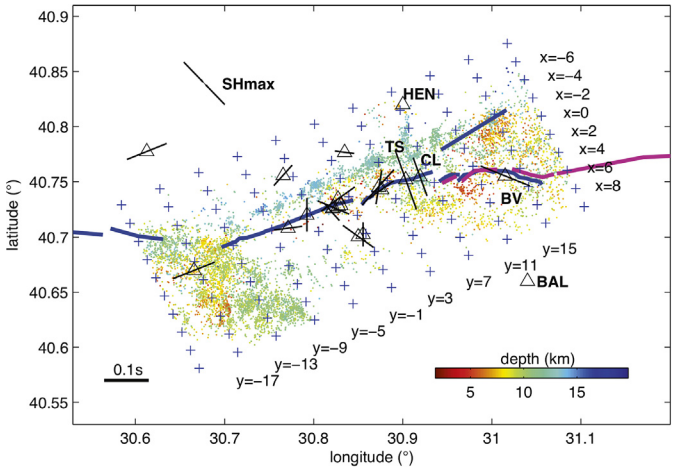

Fig. 2. Map of the distribution of events (color-coded by their depths) used in the inversion, stations (triangles), and the inversion grids (crosses). The solid bars over the stations represent the average fast direction and the delay time. The surface ruptures of the İzmit and Düzce earthquakes are indicated with thick blue and purple lines, respectively. A pair of arrows represents the regional maximum horizontal stress direction. Note that stations HEN and BAL used by Hurd and Bohnhoff (2012) are not included in the inversion. (For interpretation of the references to color in this figure legend, the reader is referred to the web version of this article.)

of ~22 000 SWS measurements were automatically calculated by a covariance matrix method of Silver and Chan (1991).

In this study, we focus on the region along the fault strike and in the immediate vicinity of the Karadere segment, which is trending ~70° to the east. The west side of the study region starts from a 5-km-long surface-rupture gap near the town of Akyazi during the İzmit earthquake (Tibi et al., 2001) (Fig. 1). The Almacik block in the south of the Karadere segment is primarily mafic and embedded with andesitic to basaltic rocks and sedimentary sequences (Yilmaz et al., 1997). To the east end of Karadere segment, the rupture bifurcated during the İzmit earthquake and stopped near the Düzce basin (Gulen et al., 2002; Fig. 1). However, the southern strand of the bifurcation partly re-ruptured during the subsequent Düzce earthquake.

Fig. 2 shows the inversion grid for the SWS tomography and the average SWS parameters at each station. Detailed rose diagrams for each station are not shown here, but can be found in Fig. 7 of Peng and Ben-Zion (2004). We choose this region because of its dense

Table 1
1D velocity model in Karadere–Düzce branch of NAF.

Layer top (km)	0.0	2.5	3.5	6.0	9.0	13.0	30.0
Vp (km/s)	3.443	5.519	5.628	5.906	6.053	6.332	8.000
Vs (km/s)	1.990	3.190	3.253	3.414	3.499	3.660	4.624

event–station coverage. The inversion coordinate system is rotated ~70° clockwise from the north so that the Y-axis is subparallel to the strike of the Karadere segment. The line $X = 0$ roughly follows the surface trace ruptured during the İzmit earthquake, and the center of the coordinate is at longitude 30.85°E and latitude 40.74°N. 20 751 SWS measurements are selected from 7856 events with their ray paths within −21 to 19 km along the Y direction (strike-parallel) and −8 to 10 km along the X direction (strike-perpendicular). The majority of the events were distributed at the depth range of 5–10 km (Fig. 2). The inversion grid nodes in the Z direction are at $Z = 0$, 2.5, 3.5, 6.0, 9.0, 13.0 and 30 km (Table 1). In this study we do not apply further selection criteria as Peng and Ben-Zion (2004) did. However, we weigh each measurement by the corresponding cross-correlation coefficient of fast and slow components in inversion in order to reduce the influence of low quality measurements.

Fig. 2 shows that most fast polarization directions for the stations on or close to the fault are parallel or subparallel to the nearby fault strike. It is interesting to find that the fast polarizations at stations TS and CL are almost perpendicular to the fault strike (Fig. 2). If the anisotropy is stress-induced and the maximum compressive stress direction is perpendicular to the fault strike, the fast polarization direction is fault-perpendicular. However, the direction of the regional maximum horizontal compressive stress is NW–SE (Bellier et al., 1997; Tadokoro et al., 2002; Görgün et al., 2010), which has a large angle against the local fault strike. Therefore, the fault-perpendicular fast polarization anomaly is not due to stress-induced anisotropy. It is likely the existence of anisotropic bodies with preferred mineral alignment could cause the fault-perpendicular polarization. It is noted that the cycle skipping arising from SWS analysis could also cause the fault-perpendicular fast polarization, where the fast and slow components are mismatched by one or more half cycles.

3. Method

The SWS tomography method developed by Zhang et al. (2007) is based on two major assumptions. First, it assumes a single-layer anisotropy model that contains vertically oriented microcracks or shear fabric and hence is azimuthal. This is common for crustal anisotropy (Crampin et al., 1978; Crampin, 1987; Boness and Zoback, 2006) and also one of the assumptions for the Silver and Chan (1991) method, which was used to obtain the measurements in this study. The second assumption is that splitting delay time is accumulated for each ray segment along the entire ray path (Fischer et al., 2000). However, the physical meaning of the measured splitting time is still vague when the anisotropy is complicated. In particular, it is not clear whether the measured delay time represents the summation of anisotropy for layers with different fast directions. The previous debate on the ability of using delay times to predict the occurrence of an earthquake also shows the ambiguity of the physical meaning of delay times (e.g., Aster et al., 1990, 1991; Crampin et al., 1991). However, based on a very simplified model given by the first assumption, the shear wave splits once when entering a single layer of azimuthally anisotropic material, and the delay times between fast and slow shear waves keep increasing when traveling through the material. In addition, Silver and Savage (1994) showed that the Silver and Chan (1991) method would produce apparent splitting measurements of the fast polarization and delay time for a two-layer anisotropy model.

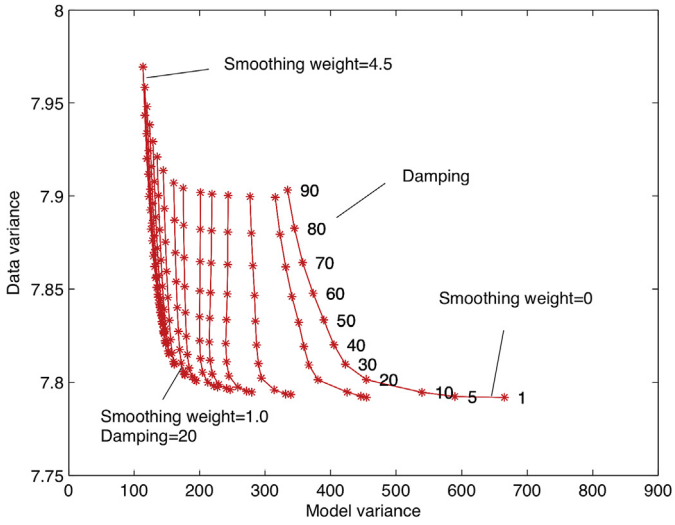

Fig. 3. L-curves of smoothing and damping parameters. The optimal pair chosen for inversion is smoothing weight = 1.0 and damping weight = 20.

As a result, the splitting times obtained from this method represent the apparent strength of the anisotropy over the entire ray path. Therefore, it is reasonable to assume that the splitting time is accumulated along the ray path for a relatively simplified model.

Based on the assumptions above, the total observed delay time δt can be expressed as

$$\delta t = \int \frac{K \cos\alpha}{V}\, dl \tag{1}$$

where α is the angle between the ray path and the vertical direction, dl is the incremental ray path, and K is the anisotropic strength. The anisotropic strength K is defined as

$$K = \frac{V_{fast} - V_{slow}}{V} \tag{2}$$

where V_{fast} and V_{slow} are the fast and slow S-wave velocities, respectively, and V is the average S-wave velocity.

In the SWS tomography program, regularization methods including damping and smoothing are introduced to stabilize the inversion. Trade-off L-curve analysis is used to search for the appropriate damping and smoothing values that balance minimizing the model variance and data variance (Fig. 3). We tested 165 pairs of damping and smoothing parameters and determined damping value of 20 and smoothing weight of 1 are suitable for this inversion (Fig. 3).

We use a simple 1D layered velocity model (Table 1; Seeber et al., 2000) to compute the ray paths for inverting the anisotropy model according to Eq. (1), although a 3D velocity model around the study region has been recently published (Koulakov et al., 2010). It is true that by using the simple 1D velocity model, the anisotropy model will be less accurate. However, the main features of the anisotropy model will be similar for both velocity models. This is because the ray paths do not differ significantly, and as a result the linear system according to Eq. (1) is also similar. A small change in the velocity will result in a proportional change in the anisotropy percentage. Considering the velocity perturbation between the 1D and 3D models is generally ~5%, the resulting change in the anisotropy percentage is also ~5%. This will have a minimum effect on the overall anisotropy patterns observed later.

4. Results

To characterize the resolution capability of the SWS tomography method in this study, we use two ways: the ray path density quantified by the Derivative Weighted Sum (DWS) for each inversion

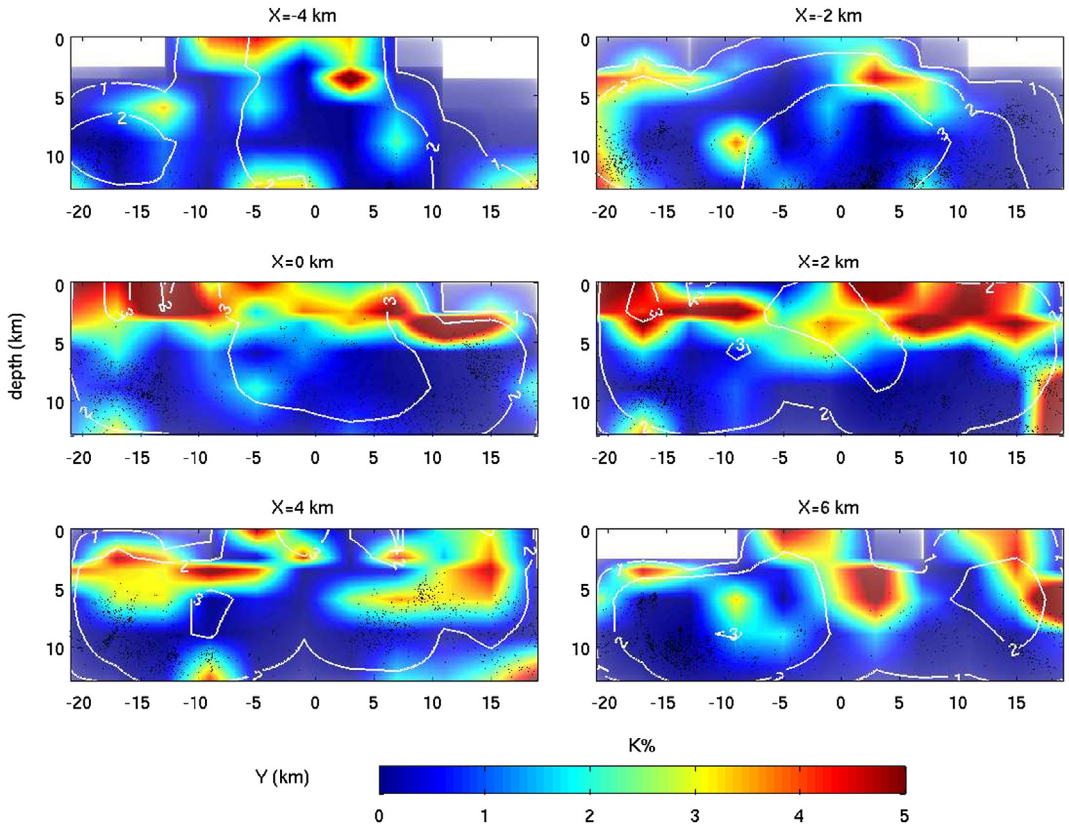

Fig. 4. Along-fault sections of anisotropy percentage at $X = -4,\ -2,\ 0,\ 2,\ 4$ and 6 km, respectively. White contours are DWS plotted in a logarithmic-based-10 scale. Black dots are events within half of the grid size of each section. Colors are weighted by the DWS values (areas with low DWS are faded and areas with high DWS are stressed). The areas without any ray path (DWS = 0) are not sampled and thus whitened.

grid node and the checkerboard resolution test. In real applications, ray-sampling density has been routinely used to qualitatively describe if the model is well resolved (e.g., Haslinger et al., 1999) although ray angular coverage information is not considered. DWS is a measure of model sampling, representing the relative density of ray paths weighted by the importance of each ray segment by its distance to the grid node (Haslinger et al., 1999). In general, the model areas with higher DWS values are better resolved (Haslinger et al., 1999; Zhang and Thurber, 2007).

Similar to the checkerboard resolution test used for velocity inversion, we also constructed a checkerboard anisotropy model with anomalies from 0 to 5% (see supplementary Figs. S1–S6). The checkerboard resolution test shows the recovery of anomalies in the regions of interest is generally acceptable (e.g., $X = 0$ and 2 in the immediate vicinity of the fault). The resolution in the deeper part of the model is higher than in the shallower part because of the better ray coverage, which is also reflected by the distribution of DWS values.

Figs. 4 and 5 show the cross-sections at different X values (along the faults trike) and horizontal slices at different depths of the 3D anisotropy percentage model, respectively. Fig. 6 shows cross-sections of the anisotropy percentage model at $Y = -9$ km and 11 km, around the center of the Karadere segment and the Düzce segment that ruptured during the İzmit and Düzce earthquakes, respectively. The anisotropy models in Figs. 4 to 6 are shown in a faded color scheme in which the areas with lower DWS values are more faded and the areas with higher DWS values are more highlighted. The areas without ray coverage (DWS = 0) are whitened. The areas of interest generally have moderate to high resolution (DWS = 10–1000, Figs. 4–6).

In the shallow crust (depth < 5 km) of the Karadere–Düzce branch of the NAF, the anisotropy is very strong (as high as 5%) and concentrates around the Karadere fault trace (e.g., $X = 0$ and $X = 2$ km). The belt-like anisotropic zone is generally shallower than 5 km, and becomes deeper to the northeast ($Y > 10$ km), close to the fault segment that was ruptured twice during the İzmit and Düzce earthquakes (Fig. 4). The anisotropy zone is mainly shifted to the SE side of the fault trace ($X = 0$–5 km) for the SW fault segment ($Y = -20$ to -5 km) (Fig. 5). Between -5 and 5 km along the Y direction, the anisotropic zone becomes more diffuse, with the highest anisotropy concentrated around the Karadere rupture zone (Fig. 5). This coincides with anomalous fast polarization directions observed at stations TS and CL between $Y = 3$ and $Y = 7$ km (Peng and Ben-Zion, 2004), and a minor step over (Hartleb et al., 2002) to the east of the Kadifekale town (at $X = 0$ and $Y = 0$ km). However, for the anomalous fault-perpendicular fast polarization, the possibility of cycle skipping cannot be ruled out. It is possible that the real fast polarization is along the fault strike while cycle skipping leads to a 90° ambiguity of fast polarization and one or more half periods increase in delay times. Further to the east ($Y = 5$–19 km), the anisotropy zone is mainly centered around the rupture zones of the İzmit and Düzce earthquakes at shallow depths (slice $Z = 2.5$ km and $Z = 3.5$ km of Fig. 5). Another high anisotropy zone is observed from the surface down to the depth of 6 km to the NW side of the surface rupture zone near station BV ($X = 0$ km), where the maximum delay times of up to 0.3 s were observed.

At $Y = -9$ km around the center of the Karadere segment that ruptured during the İzmit earthquake, the anisotropy extends discontinuously from the near surface to the depth around 12 km, with a broken zone around the depth of 5 km (Fig. 6). Overall, the dipping trend of the anisotropy zone follows closely to the fault dip angle of the Karadere segment, which is approximately 80° to the north (Ben-Zion et al., 2003; Bulut et al., 2007). However, the

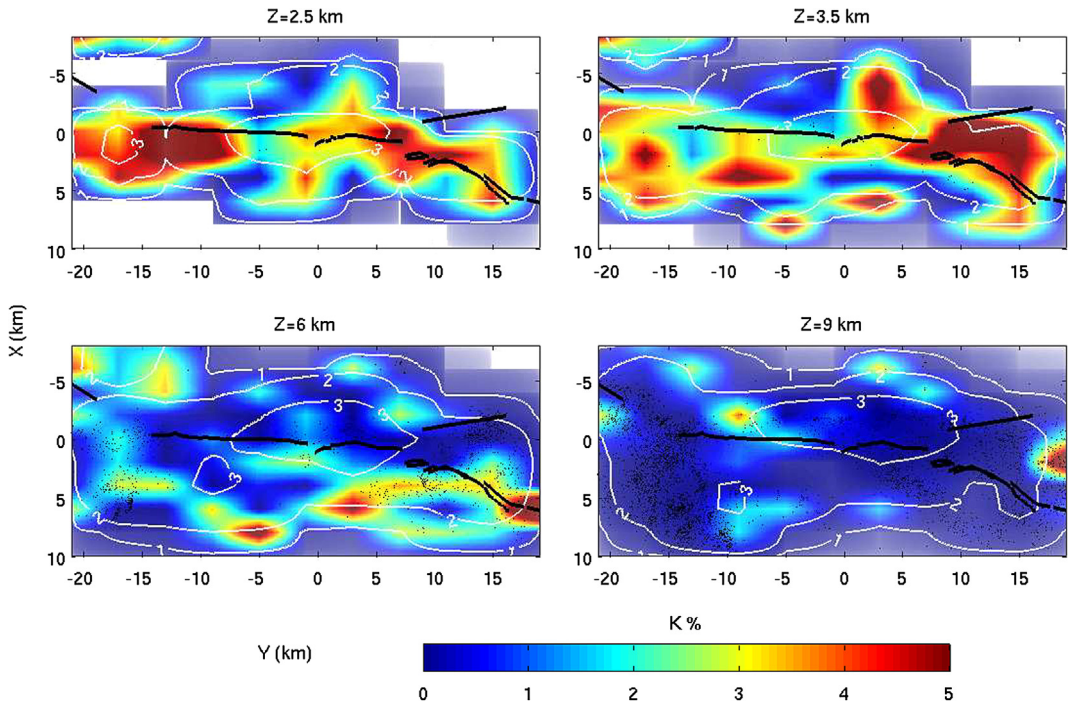

Fig. 5. Horizontal sections of anisotropy percentage at $Z = 2.5$, 3.5, 6 and 9 km, respectively. Black lines are the projected fault surface traces of Karadere and Düzce segments. Other symbols and notations are the same as in Fig. 4.

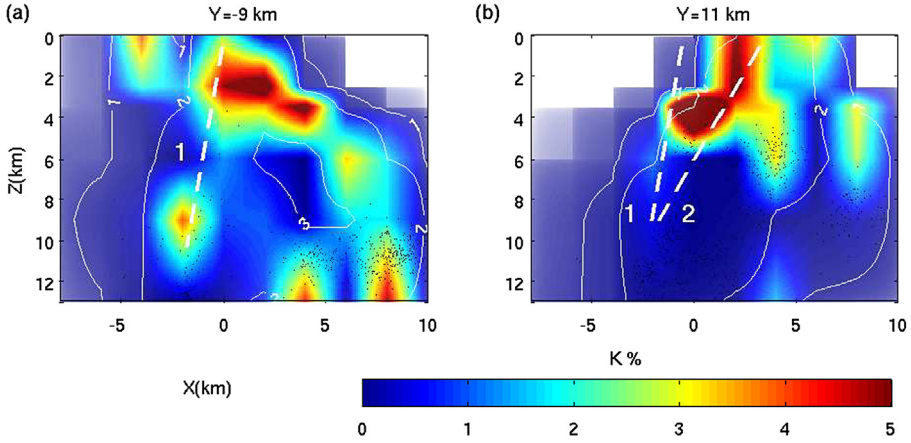

Fig. 6. Cross-sections of anisotropy percentage in (a) northeast-trend Karadere segment and (b) near east-trend Düzce segment. Black dots represent the events within half of grid size at the section. (a) The white dashed line 1 indicates the rupture dip of the Karadere segment. The white dashed line 2 indicates the rupture dip of Düzce segment. Other symbols and notations are the same as in Fig. 4.

strongest anisotropy is localized within the Almacik block to the SE side of the fault, which is also shown in Fig. 4. At $Y = 11$ km around the western end of the segment that ruptured during the Düzce earthquake, the anisotropy greater than 5% is mainly concentrated from 2 to 6 km in depth and between the extension of the Karadere segment and the Düzce segment that ruptured twice (Fig. 6). The anisotropy zone dips about 50° to the north, close to the dipping angle (50–70° to the north) of the Düzce mainshock rupture and its aftershocks (Burgmann et al., 2002). The coincidence of these anisotropic zones with the fault geometries indicates that they are strongly structure-related.

In addition to these strong anisotropy anomalies around active rupture zones at shallow depths, we also observe pockets of isolated anisotropy anomalies at greater depths away from the faults. They are generally at the dimension of kilometers in radii and have comparable anisotropy percentage with the belt-like anisotropic zone in the fault zone.

5. Discussion

Peng and Ben-Zion (2004) only selected events that are within the shear-wave window (i.e., the epicentral distance less than the depth) for measuring their SWS parameters. If the subsurface velocity structure is uniform, this corresponds to an incidence angle of 45°. However, because of the lower velocity near the surface, the rays tend to be more vertical as the ray approaches to the surface. For the anisotropy tomography in this study, as the velocity tomography, it also relies on the crossing rays to image the anisotropy structure. As a result, the model resolution in the shallower depths is relatively worse, as shown in the checkerboard resolution test in the supplementary material.

Nevertheless, due to the dense distribution of earthquakes and thus good ray coverage in our study area, we were able to determine the 3D anisotropy distribution around the Karadere–Düzce branch of the NAF with a reasonable resolution. In summary, we found that the anisotropy is primarily distributed in a continuous

belt-like zone down to 3–5 km in depth and of 1–3 km wide along the Karadere–Düzce segment of the NAF. In the deeper region and away from the faults, the anisotropy shows isolated blocks but with comparable anisotropy percentage. The distinct anisotropy features in and outside the fault zones provide a unique opportunity to understand the anisotropy mechanisms in the upper crust of the study region.

Because of the relative movement of blocks on both sides of the fault, it generally causes the shear fabric or microfractures that are preferentially aligned parallel to fault zones (Boness and Zoback, 2006). Such a preferential alignment would result in fault-parallel fast polarization. In addition, the belt-like anisotropic zone generally follows the surface fault trace (Fig. 4), which strongly indicates a structure-controlled mechanism of crustal anisotropy in this region.

We note that the rotation of maximum horizontal compression near the fault may introduce some potential bias when using fast polarization to infer anisotropy mechanisms. For example, Holt et al. (2013) used the aftershock data of the Darfield earthquake to invert regional stress field in New Zealand. They found that the maximum horizontal compression rotated to be parallel to the Darfield fault, where fault-parallel fast polarizations were observed for some on-fault stations (Syracuse et al., 2012). However, this rotation has not been observed for the 1999 İzmit earthquake (Görgün et al., 2010).

The width of anisotropy zone is confined within 3 km near the fault interface, which is much wider than the 100–300 m of low-velocity damage zone inferred from fault zone trapped waves (e.g., Ben-Zion et al., 2003; Peng et al., 2003; Li et al., 2006). It is quite possible that fault zone trapped waves required a coherent low-velocity zone that only exists in the immediate vicinity of the fault interface, while fault-zone related fractures could exist at much further distances. We also note that previous studies of fault zone trapped waves were primarily based on seismic data collected by dense fault zone arrays with a typical length of a few hundred meters. Hence, it is possible that a much wider damage zone exists, but was not detected by a relatively short array. Indeed, using a 5-km long dense array, Cochran et al. (2009) found a 1.5-km wide damage zone along the Calico fault in the eastern California shear zone.

It is interesting to note that the anisotropic zone on the Karadere segment is asymmetric rather than centered with respect to the fault trace (Figs. 5 and 6). The damage zone is ∼3 km wide and localized to the south of the fault surface trace, while the Karadere segment is dipping approximately 80° to the north. Such asymmetric localization of the damage zone may result from varying intensity of hydrothermal conditions and/or rock properties of both walls (Sibson, 2003). Alternatively, an asymmetric damage zone is expected for dynamic ruptures propagating along a fault interface that separates different elastic media (Ben-Zion and Shi, 2005). Such ruptures would propagate preferably in the direction of slip on the slower side of the fault, and produce tensile radiations and damages on the faster side of the fault (Ben-Zion, 2001; Shi and Ben-Zion, 2006; Bulut et al., 2012). The Almacik block in the SE side of the fault has a higher velocity than the sedimentary basin on the other side, at least in the top few kilometers (Koulakov et al., 2010). Such assumption is qualitatively consistent with the eastward propagation (slip direction of the slow side) of the İzmit rupture along the Karadere segment, and additional fractures and anisotropy in the faster Almacik block.

However, the pattern becomes much more complicated to the east of the town of Kadifekale, where the rupture bifurcated and finally stopped near Golyaka during the İzmit earthquake (Figs. 1 and 5). 87 days after the İzmit earthquake, the November Düzce earthquake re-ruptured part of northeastern section of the Karadere segment, and the remaining segment to the city of Bulu. Such an unusual rupture process indicates strong complexity of rock properties and heterogeneity of stress field. For example, Hurd and Bohnhoff (2012) showed a bimodal pattern of fast polarization directions at station HEN located toward the eastern part of the İzmit rupture and close to the Karadere fault ($X = -6$ km and $Y = 7$ km), which is close to the fault-zone anisotropy body imaged in this study. Further to the east near the Düzce basin, our results indicate that the anisotropic zone might be controlled by both the Karadere segment and the Düzce segment (Fig. 6b). Görgün et al. (2010) showed that the Düzce fault that bounds the Düzce basin may represent a major asperity which was activated by the east end of the İzmit rupture but not ruptured until three months later. Although the stress imparted from the İzmit rupture to the Düzce fault was complicated, the asperity that was ruptured afterwards may induce additional damage and hence contribute to the high anisotropy between two segments.

The continuous anisotropic zone is generally 3–5 km deep, which is compatible with the results implied from the distribution pattern of the delay times and event locations (e.g., Peng and Ben-Zion, 2004; Hurd and Bohnhoff, 2012). This is also the typical depth extent of anisotropy reported in other fault zones (e.g., Zhang and Schwartz, 1994; Liu et al., 2004). Because the cracks are expected to close and/or reduce in density due to the increase of confining pressure with depth, we would expect to observe a reduction of anisotropy with depth. It is also reported that the fault zone might change at 3 km depth from a mechanically passive zone in the shallow part to an earthquake prone zone in the deeper part (Dieterich, 1979; Marone and Scholz, 1988; Blanpied et al., 1991). However, we note that the anisotropy belt extends as deep as 6 km in the northeast (Fig. 6b), where the fault correspondingly ruptured during both the İzmit and Düzce earthquakes. Coincidently, this region also shows the highest anisotropy in our study area, consistent with the finding that station BV recorded one of the largest delay times (Peng and Ben-Zion, 2004). Maximum afterslip was also observed in this region from GPS data after the İzmit and before the Düzce earthquake (Burgmann et al., 2002). Therefore, the fault that had been ruptured by both earthquakes may get additional damages at greater depths, resulting in stronger anisotropy.

Away from the fault, the anisotropy is generally smaller and decreases to 0–1% in the shallow part. However, in the deeper part (> ∼4 km), there are several strong but isolated anisotropic blocks embedded in the weak anisotropic background. For example, in the Almacik block there are several highly anisotropic blocks located at the depth of 6–10 km in the immediate vicinity of the aftershock zone. This is consistent with the inference by Hurd and Bohnhoff (2012) that the anisotropy beneath the station BAL (Fig. 2) located near the center of the Almacik block may lie close to the source region instead of right beneath the station. Note that the SWS observations on station BAL are not included in our study, thus providing an independent support of our tomography results. As found previously, extrusive igneous and sedimentary rocks are embedded in the mafic Almacik block (Yilmaz et al., 1997). Therefore we suggest that these isolated anisotropic blocks outside the fault zone are likely due to local lithology. The candidate mechanisms for the highly anisotropic bodies outside the fault zone include the preferential aligned minerals in igneous rocks, foliation and/or saturation of fluids in sedimentary rocks. If seismic anisotropy outside the fault zone is due to stress-controlled fractures, the fast polarization direction is expected to align with the direction of maximum compressive stress. However, previous studies show fast polarization directions outside the fault zone vary with stations and some of them are neither parallel to the maximum compressive stress direction or along the fault strike (Peng and Ben-Zion, 2004; Hurd and Bohnhoff, 2012). Therefore, these isolated anisotropic

anomalies are more likely caused by individual igneous rock bodies with different minerals alignment directions.

6. Conclusions

We applied the 3D SWS tomography method developed by Zhang et al. (2007) to image the upper crustal anisotropy in the Karadere–Düzce branch of the NAF. The tomography benefited from the large dataset that sampled the study area with high coverage. The results show strong spatial heterogeneity of anisotropy on and outside the fault zone. A continuous belt-like highly anisotropic zone is identified along the fault, generally ~3 km wide and down to ~5 km, which is generally consistent with previous studies on shallow crust anisotropy in the NAF and the San Andreas Fault (e.g., Ben-Zion et al., 2003; Zhang et al., 2007). The observed asymmetric pattern of anisotropy along the Karadere segment is qualitatively consistent with asymmetric damages from the unilateral eastward propagation of the İzmit rupture (Shi and Ben-Zion, 2006). The strongest anisotropy zone in the study region is coincident with the segment ruptured twice during the İzmit and Düzce earthquakes. These results, together with fault-parallel fast polarization directions around the fault, strongly support the mechanism of the structure-controlled anisotropy due to aligned fabric related to fault damage zone. In the deeper part of the fault zone, anisotropy generally becomes very weak because of the closure of fractures, as a result of fault healing and increased confining stress with depth. However, in the deeper part outside the fault zone we found several highly anisotropic bodies in form of isolated blocks that are embedded in the low anisotropy background. Our results explain the inconsistent fast shear-wave polarization directions varying with stations outside the fault zone that was found in previous studies. The isolated anisotropy blocks outside the fault zone could be explained by individual intrusive igneous rock bodies with different mineral alignments. In summary, seismic anisotropy in upper crust of the Karadere–Düzce branch of the NAF is structurally controlled.

Acknowledgements

We thank the editor Peter Shearer and two anonymous reviewers for their constructive comments that helped to improve the manuscript significantly. This work is supported by China's State Administration of Foreign Experts Affairs International Partnership Program for Creative Research Teams, and the National Science Foundation (EAR-0908310).

Appendix A. Supplementary material

Supplementary material related to this article can be found online at http://dx.doi.org/10.1016/j.epsl.2014.01.046.

References

Abt, D., Fischer, K., 2008. Resolving three-dimensional anisotropic structure with shear wave splitting tomography. Geophys. J. Int. 173, 859–886.
Aster, R., Shearer, P., Berger, J., 1990. Quantitative measurements of shear-wave polarizations at the Anza Seismic Network, southern California – Implications for shear-wave splitting and earthquake prediction. J. Geophys. Res., Solid Earth Planets 95, 12449–12473.
Aster, R., Shearer, P., Berger, J., 1991. Comment on "Quantitative measurements of shear-wave polarizations at the Anza Seismic Network, southern California – Implications for shear-wave splitting and earthquake prediction" by Aster, Richard C., Shearer, Peter M., Berger, John – Reply. J. Geophys. Res., Solid Earth Planets 96, 6415–6419.
Audoine, E., Savage, M.K., Gledhill, K., 2004. Anisotropic structure under a back arc spreading region, the Taupo Volcanic Zone, New Zealand. J. Geophys. Res. 109, B11305. http://dx.doi.org/10.1029/2003JB002932.
Bellier, O., Over, S., Poisson, A., Andrieux, J., 1997. Recent temporal change in the stress state and modern stress field along the North Anatolian Fault Zone (Turkey). Geophys. J. Int. 131, 61–86.
Ben-Zion, Y., 2001. Dynamic ruptures in recent models of earthquake faults. J. Mech. Phys. Solids 49, 2209–2244.
Ben-Zion, Y., Peng, Z., Okaya, D., Seeber, L., Armbruster, J., Ozer, N., Michael, A., Baris, S., Aktar, M., Kuwahara, Y., Ito, H., 2003. A shallow fault-zone structure illuminated by trapped waves in the Karadere–Düzce branch of the North Anatolian Fault, western Turkey. Geophys. J. Int. 152, 699–717.
Ben-Zion, Y., Shi, Z., 2005. Dynamic rupture on a material interface with spontaneous generation of plastic strain in the bulk. Earth Planet. Sci. Lett. 236, 486–496.
Blanpied, M., Lockner, D., Byerlee, J., 1991. Fault stability inferred from granite sliding experiments at hydrothermal conditions. Geophys. Res. Lett. 18, 609–612.
Boness, N., Zoback, M., 2006. Mapping stress and structurally controlled crustal shear velocity anisotropy in California. Geology 34, 825–828.
Bulut, F., Ben-Zion, Y., Bohnhoff, M., 2012. Evidence for a bimaterial interface along the Mudurnu segment of the North Anatolian Fault Zone from polarization analysis of P waves. Earth Planet. Sci. Lett. 327, 17–22.
Bulut, F., Bohnhoff, M., Aktar, M., Dresen, G., 2007. Characterization of aftershock-fault plane orientations of the 1999 İzmit (Turkey) earthquake using high-resolution aftershock locations. Geophys. Res. Lett. 34, L20306. http://dx.doi.org/10.1029/2007GL031154.
Burgmann, R., Ergintav, S., Segall, P., Hearn, E., McClusky, S., Reilinger, R., Woith, H., Zschau, J., 2002. Time-dependent distributed afterslip on and deep below the İzmit earthquake rupture. Bull. Seismol. Soc. Am. 92, 126–137.
Cochran, E., Li, Y., Shearer, P., Barbot, S., Fialko, Y., Vidale, J., 2009. Seismic and geodetic evidence for extensive, long-lived fault damage zones. Geology 37, 315–318.
Crampin, S., 1987. A review of extensive-dilatancy anisotropy (EDA) in hydrocarbon reservoirs. Geophys. J. R. Astron. Soc. 89, 463.
Crampin, S., 1990. Seismic anisotropy in the Earth's crust – A citation-classic commentary on a review of wave motion in anisotropic and cracked elastic-media. Phys. Chem. Earth Sci. 30, 40, 18.
Crampin, S., 1991. Seismic anisotropy due to preferred mineral orientation observed in shallow crustal rocks in southern Alaska – Comment. Geology 19, 859.
Crampin, S., Bamford, D., Mcgonigle, R., 1978. Estimating crack parameters by inversion of P-wave velocity–anisotropy. Geophys. J. R. Astron. Soc. 53, 173.
Crampin, S., Booth, D., 1985. Shear-wave polarizations near the North Anatolian Fault. 2. Interpretation in terms of crack-induced anisotropy. Geophys. J. R. Astron. Soc. 83, 75–92.
Crampin, S., Booth, D., Evans, R., Peacock, S., Fletcher, J., 1991. Comment on "Quantitative measurements of shear-wave polarizations at the Anza Seismic Network, southern California – Implications for shear-wave splitting and earthquake prediction" by Aster, Richard C., Shearer, Peter M., and Berger, John. J. Geophys. Res., Solid Earth Planets 96, 6403–6414.
Dieterich, J., 1979. Modeling of rock friction. 1. Experimental results and constitutive equations. J. Geophys. Res. 84, 2161–2168.
Eken, T., Bohnhoff, M., Bulut, F., Can, B., Aktar, M., 2013. Crustal anisotropy in the eastern Sea of Marmara region in northwestern Turkey. Bull. Seismol. Soc. Am. 103, 911–924.
Evans, R., Crampin, S., Booth, D., 1985. Shear-wave polarizations. 1. Observations near the North Anatolian Fault (NAF). Geophys. J. R. Astron. Soc. 81, 340–341.
Fischer, K., Parmentier, E., Stine, A., Wolf, E., 2000. Modeling anisotropy and plate-driven flow in the Tonga subduction zone back arc. J. Geophys. Res., Solid Earth 105, 16181–16191.
Fukao, Y., 1984. Evidence from core-reflected shear-waves for anisotropy in the Earth's mantle. Nature 309, 695–698.
Görgün, E., Bohnhoff, M., Bulut, F., Dresen, G., 2010. Seismotectonic setting of the Karadere–Düzce branch of the North Anatolian Fault Zone between the 1999 Izmit and Düzce ruptures from analysis of Izmit aftershock focal mechanisms. Tectonophysics 482, 170–181.
Gulen, L., Pinar, A., Kalafat, D., Ozel, N., Horasan, G., Yilmazer, M., Isikara, A., 2002. Surface fault breaks, aftershock distribution, and rupture process of the 17 August 1999 İzmit, Turkey, earthquake. Bull. Seismol. Soc. Am. 92, 230–244.
Hartleb, R., Dolan, J., Akyuz, H., Dawson, T., Tucker, A., Yerli, B., Rockwell, T., Toraman, E., Cakir, Z., Dikbas, A., Altunel, E., 2002. Surface rupture and slip distribution along the Karadere segment of the 17 August 1999 İzmit and the western section of the 12 November 1999 Düzce, Turkey, earthquakes. Bull. Seismol. Soc. Am. 92, 67–78.
Haslinger, F., Kissling, E., Ansorge, J., Hatzfeld, D., Papadimitriou, E., Karakostas, V., Makropoulos, K., Kahle, H., Peter, Y., 1999. 3D crustal structure from local earthquake tomography around the Gulf of Arta (Ionian region, NW Greece). Tectonophysics 304, 201–218.
Holt, R., Savage, M., Townend, J., Syracuse, E., Thurber, C., 2013. Crustal stress and fault strength in the Canterbury Plains, New Zealand. Earth Planet. Sci. Lett. 383, 173–181.
Hurd, O., Bohnhoff, M., 2012. Stress- and structure-induced shear-wave anisotropy along the 1999 Izmit rupture, northwest Turkey. Bull. Seismol. Soc. Am. 102, 2177–2188.
Koulakov, I., Bindi, D., Parolai, S., Grosser, H., Milkereit, C., 2010. Distribution of seismic velocities and attenuation in the crust beneath the North Anatolian Fault (Turkey) from local earthquake tomography. Bull. Seismol. Soc. Am. 100, 207–224.

Leary, P., Crampin, S., Mcevilly, T., 1990. Seismic fracture anisotropy in the Earth's crust – an overview. J. Geophys. Res., Solid Earth Planets 95, 11105–11114.
Li, Y., Chen, P., Cochran, E., Vidale, J., Burdette, T., 2006. Seismic evidence for rock damage and healing on the San Andreas fault associated with the 2004 M 6.0 Parkfield earthquake. Bull. Seismol. Soc. Am. 96, S349–S363.
Liu, E., Queen, J., Li, X., Chapman, M., Maultzsch, S., Lynn, H., Chesnokov, E., 2003. Observation and analysis of frequency-dependent anisotropy from a multicomponent VSP at Bluebell–Altamont Field, Utah. J. Appl. Geophys. 54, 319–333.
Liu, Y., Teng, T., Ben-Zion, Y., 2004. Systematic analysis of shear-wave splitting in the aftershock zone of the 1999 Chi-Chi, Taiwan, earthquake: Shallow crustal anisotropy and lack of precursory variations. Bull. Seismol. Soc. Am. 94, 2330–2347.
Liu, Y., Zhang, H., Thurber, C., Roecker, S., 2008. Shear wave anisotropy in the crust around the San Andreas Fault near Parkfield: spatial and temporal analysis. Geophys. J. Int. 172, 957–970.
Long, M., de Hoop, M., van der Hilst, R., 2008. Wave-equation shear wave splitting tomography. Geophys. J. Int. 172, 311–330.
Marone, C., Scholz, C., 1988. The depth of seismic faulting and the upper transition from stable to unstable slip regimes. Geophys. Res. Lett. 15, 621–624.
Peng, Z., Ben-Zion, Y., 2004. Systematic analysis of crustal anisotropy along the Karadere–Düzce branch of the North Anatolian fault. Geophys. J. Int. 159, 253–274.
Peng, Z., Ben-Zion, Y., Michael, A., Zhu, L., 2003. Quantitative analysis of seismic fault zone waves in the rupture zone of the 1992 Landers, California, earthquake: evidence for a shallow trapping structure. Geophys. J. Int. 155, 1021–1041.
Seeber, L., Armbruster, J.G., Ozer, N., Aktar, M., Baris, S., Okaya, D., Ben-Zion, Y., Field, E., 2000. The 1999 earthquake sequence along the North Anatolia transform at the juncture between the two main ruptures. In: Barka, et al. (Eds.), The 1999 İzmit and Düzce Earthquakes: Preliminary Results. Istanbul Technical University, pp. 209–223.
Shi, Z., Ben-Zion, Y., 2006. Dynamic rupture on a bimaterial interface governed by slip-weakening friction. Geophys. J. Int. 165, 469–484.
Shih, X., Meyer, R., Schneider, J., 1989. An automated, analytical method to determine shear-wave splitting. Tectonophysics 165, 271–278.
Sibson, R., 2003. Thickness of the seismic slip zone. Bull. Seismol. Soc. Am. 93, 1169–1178.
Silver, P., Chan, W., 1991. Shear-wave splitting and subcontinental mantle deformation. J. Geophys. Res., Solid Earth 96, 16429–16454.
Silver, P., Savage, M., 1994. The interpretation of shear-wave splitting parameters in the presence of 2 anisotropic layers. Geophys. J. Int. 119, 949–963.
Syracuse, E., Holt, R., Savage, M., Johnson, J., Thurber, C., Unglert, K., Allan, K., Karaliyadda, S., Henderson, M., 2012. Temporal and spatial evolution of hypocentres and anisotropy from the Darfield aftershock sequence: implications for fault geometry and age. N.Z. J. Geol. Geophys. 55, 287–293.
Tadokoro, K., Ando, M., Baris, S., Nishigami, K., Nakamura, M., Ucer, S., Ito, A., Honkura, Y., Isikara, A., 2002. Monitoring of fault healing after the 1999 Kocaeli, Turkey, earthquake. J. Seismol. 6, 411–417.
Thurber, C., Zhang, H., Waldhauser, F., Hardebeck, J., Michael, A., Eberhart-Phillips, D., 2006. Three-dimensional compressional wavespeed model, earthquake relocations, and focal mechanisms for the Parkfield, California, region. Bull. Seismol. Soc. Am. 96, S38–S49.
Tibi, R., Bock, G., Xia, Y., Baumbach, M., Grosser, H., Milkereit, C., Karakisa, S., Zunbul, S., Kind, R., Zschau, J., 2001. Rupture processes of the 1999 August 17 İzmit and November 12 Düzce (Turkey) earthquakes. Geophys. J. Int. 144, F1–F7.
Yang, Z., Sheehan, A., Shearer, P., 2011. Stress-induced upper crustal anisotropy in southern California. J. Geophys. Res. 116, B02302. http://dx.doi.org/10.1029/2010JB007655.
Yilmaz, Y., Tuysuz, O., Yigitbas, E., Genc, S.C., Sengor, A.M.C., 1997. Geology and tectonic evolution of the Pontides. In: Robinson, A.G. (Ed.), Regional and Petroleum Geology of the Black Sea and Surrounding Region. In: AAPG Memoirs, vol. 68. AAPG, Tulsa, OK, USA, pp. 183–226.
Zhang, H., Liu, Y., Thurber, C., Roecker, S., 2007. Three-dimensional shear-wave splitting tomography in the Parkfield, California region. Geophys. Res. Lett. 34, L24308. http://dx.doi.org/10.1029/2007GL031951.
Zhang, Z., Schwartz, S., 1994. Seismic anisotropy in the shallow crust of the Loma-Prieta segment of the San-Andreas fault system. J. Geophys. Res., Solid Earth 99, 9651–9661.
Zhang, H., Thurber, C., 2007. Estimating the model resolution matrix for large seismic tomography problems based on Lanczos bidiagonalization with partial reorthogonalization. Geophys. J. Int. 170, 337–345.